Journal of Applied Fluid Mechanics, Vol. 18, No. 11, pp. 2680-2696, 2025.
Available online at www.jafmonline.net, ISSN 1735-3572, EISSN 1735-3645.
https://doi.org/10.47176/jafm.18.11.3575

Multi-objective Optimization of Micro Wind Generator Blade Structure Parameters based on Response Surface Methodology and Non-dominated Sorting Genetic Algorithm III

C. Wang[1,2†], D. Y. Luo[2,3], H. L. Fan[1,2], H. Yang[1,2] and T. L. Wei[1,2]

[1] *College of Mechanical and Vehicle Engineering, Bengbu University, Bengbu, Anhui, 233030, China*
[2] *Anhui Province Additive Manufacturing Engineering Research Center, Bengbu University, Bengbu, Anhui, 233030, China*
[3] *College of Intelligent Manufacturing, Anhui Science and Technology University, Bengbu, Anhui, 233030, China*

†*Corresponding Author Email: wangchao1990@bbc.edu.cn*

ABSTRACT

This study investigates the effect of blade structural parameters on the power generation performance—specifically output current and voltage of a micro wind generator, using experimental testing and multi-objective optimization. The influence of blade diameter (*BD*), blade inclination angle (*BA*), blade number (*BN*), and blade root draft angle (*BRA*) on generator performance is analyzed. The Box-Behnken Design (BBD) of response surface methodology (RSM) is employed to assess variance and to establish a quadratic polynomial model linking structural parameters to performance metrics. Computational fluid dynamics (CFD) simulations are used to interpret experimental observations. The NSGA-III algorithm is applied to optimize the parameter set. Results indicate that *BRA* has negligible effect on performance. The ranking of influence on output current and voltage is *BN* > *BA* > *BD*, and on blade weight is *BN* > *BD* > *BA*. The optimal configuration comprises a *BD* of 105 mm, an inclination angle of 35.92°, and 6 blades. Validation by experiment and CFD confirms that this configuration yields higher output current and voltage with only a modest increase in blade weight, providing practical guidance for the structural design of micro wind generators.

Article History

Received April 1, 2025
Revised June 24, 2025
Accepted July 1, 2025
Available online September 3, 2025

Keywords:

Wind energy
Blade design
Box-Behnken design
Computational fluid dynamics
Response surface methodology
Non-dominated sorting algorithm

1. INTRODUCTION

Resource depletion and environmental pollution present significant challenges to economic and social development. Countries worldwide are increasingly exploring the use of emerging clean energy sources to address these issues (Rocha et al., 2018). Wind power, as a prominent clean energy source, has a considerably lower environmental effect compared to traditional thermal power generation (Sunderland et al., 2016; Kumar & Prakash, 2023). Additionally, wind energy experiences reduced transmission losses and offers greater generation efficiency than solar energy. Wind power technology has seen widespread adoption globally. According to China Financial Network, by the end of October 2024, China's cumulative installed wind power capacity is projected to exceed 500 million kilowatts, representing nearly 50% of the global total installed capacity. Furthermore, in the first quarter of 2024, China generated 266.5 billion kilowatt-hours (kWh) of wind power, which constituted 10.81% of the country's total electricity generation.

Various types of wind generators exist, with large, three-blade models being the most prevalent. These generators typically reach heights of 150 to 200 meters, with blade lengths ranging from 60 to 120 meters. However, large wind generators are associated with high production costs, expensive maintenance, and substantial investment requirements, limiting their application primarily to public power generation (Araújo et al., 2021; De Oliveira et al., 2021). The electricity generated by wind generators must be converted before integration into the grid, categorizing these generators as part of the national infrastructure. While large wind generators demonstrate high power generation efficiency, their deployment in urban, rural, and other low-wind-speed regions remains constrained. This limitation primarily arises from suboptimal economic performance, particularly regarding input-output efficiency (Tiam Kapen et al., 2022). Therefore, there is a pressing need to reduce the size of these generators and develop small or micro-scale, low-cost wind generators suitable for rural areas and urban

NOMENCLATURE

BD	Blade Diameter	T_n	composite population
BA	Blade Inclination Angle	n	generation
BN	number of blades	F_w	direct wind force
BRA	Blade Root Draft Angle	F_p	normal thrust
C_g	generator output current	F_c	tangential force
V_g	generator output voltage	**Abbreviation**	
W_b	blade weight	RSM	Response Surface Methodology
Y(X)	target response values	NSGA-II	Non-dominated Sorting Genetic Algorithm II
X	independent variables	NSGA-III	Non-dominated Sorting Genetic Algorithm III
α_0	intercept term	CFD	Computational Fluid Dynamics
α_i	first-order coefficients	FDM	Fused Deposition Modeling
α_{ij}	interaction term coefficients	PLA	Polylactic Acid
α_{ii}	quadratic term coefficients	DC	Direct Current
k	number of experimental variables	BBD	Box-Behnken Design
R_n	initial population	PEI	Polyetherimide
M	population size	CCD	Central Composite Design
S_n	offspring population	ANOVA	Analysis of Variance

high-rise buildings (Bourne et al., 2013; Akour et al., 2018).

Small wind generators can partially replace household power supplies or serve as supplementary sources to the universal power grid. A significant number of studies have been conducted on small wind generators. Sant et al. (2020) designed a nine-blade generator featuring a segmented blade structure, dividing the blade into four sections: the root at the hub end, shells with spar caps, a single shear web (with and without fillers), and the blade tip. Each section utilizes a different material and structural designs (utilizing adhesive fixation with resin) to meet specific requirements for strength and weight. Vedovelli et al. (2022) investigated the effect of blade count on the dynamic response of generators. Experimental results indicate that, compared to the three-blade configuration, the five-blade design sustains higher efficiency at low wind speeds and mitigates the risk of high-amplitude vibrations. Shen et al. (2016) optimized the aerodynamic performance of a small, three-bladed wind generator, demonstrating that the aerodynamic efficiency of small horizontal-axis wind generators is significantly influenced by their geometric design. They further emphasized that wind generator design involves a complex, multi-objective optimization process, which must account for both blade geometry and operating conditions.

Previous research has demonstrated that blade structure critically affects the power generation efficiency of generators, necessitating carefully engineered blades to effectively convert wind energy into electrical energy (Shen et al., 2016; Rocha et al., 2018; Sant et al., 2020; Vedovelli et al., 2022). However, the blade designs of small wind generators often mirror those of larger generators, resulting in complex structures, challenging manufacturing processes, and high-quality standards. These factors limit their application in everyday contexts due to specialized technical requirements. In modern high-rise buildings and rural agricultural applications, wireless remote sensors are extensively deployed to monitor environmental parameters, such as temperature, humidity, and light intensity. These sensors require relatively low power, typically below 10 mW. Connecting each sensor to the power grid would significantly increase wiring costs, including energy conversion expenses (Marin et al., 2016). In the case of battery-powered supplies, replacements will be necessary after a certain period, leading to considerable labor costs (Huda et al., 2022). From an energy cost perspective, solar power systems still require substantial economic investment. Therefore, developing a miniature wind power generation system to supply power for these devices is essential.

The efficiency of power generation in micro wind generators is inherently limited. From a cost-effective deployment perspective, optimizing their blade structure without altering the system's overall composition can significantly enhance wind energy capture efficiency. Leung et al. (2011) conducted a parametric study on the performance of a micro wind generator designed for harnessing wind energy in urban and rural environments. After CFD simulation-based optimization, they identified that a five-bladed micro wind generator with a blade inclination angle (*BA*) of 60° exhibited a relatively high power coefficient. Umar et al. (2020) examined the influence of micro-generator blades made from PVC and rubber materials on wind energy capture and power output. They conducted tests on five configurations, each with 2 to 4 blades of varying diameters; however, the results did not definitively identify a superior blade structure. According to existing literature, research on blade structure optimization for micro generators remains limited. While numerous studies emphasize the significance of blade structural parameters, targeted investigations are still lacking. Specifically, comparative analyses examining the relationship between critical parameters, such as blade count and inclination angle, and their effects on the power generation performance of micro generators with blade diameters (*BD*) of 200 mm or less are scarce.

This study examines a ring-shaped micro wind generator blade as the subject of investigation (Leung et

al., 2011). In the design phase, the overall blade structure was simplified by transforming the complex curved surface into a planar structure with uniform wall thickness. The selected structural parameter variables included *BD*, *BA*, blade number (*BN*), and blade root draft angle (*BRA*). Additive manufacturing technology, specifically fused deposition modeling (FDM) , was employed to fabricate the physical blades using polylactic acid (PLA) material (Akour et al., 2018; Suresh et al., 2024). The output current and voltage of a micro DC generator (Marin et al., 2016) were measured, and blade weight was also considered a critical metric. Preliminary observations indicated that variations in structural parameters affect not only aerodynamic performance but also the blade's mass, which may influence rotational inertia and power generation efficiency. Thus, blade weight was incorporated as an additional factor to facilitate a more comprehensive interpretation of the performance effects of structural modifications. Experimental testing was carried out to elucidate the relationships between the variables and target metrics. Utilizing single-factor experiments, the Box-Behnken design (BBD) from response surface methodology (RSM) (Zuo et al., 2023; Mi et al., 2024) was employed to derive equations that characterize the relationships between structural variables and target metrics, and to analyze the influence of each variable on the target metrics, as well as the interactions among them. Furthermore, the derived equations underwent multi-objective optimization through the improved third-generation non-dominated sorting genetic algorithm (NSGA-III) (Deb & Jain, 2014; Liu et al., 2019; Gu et al., 2022; Deng et al., 2024), yielding predicted optimal targets and corresponding parameter values. Finally, experiments were conducted using the optimized parameters to validate both the effectiveness of the optimization and the accuracy of the predictions. This research serves as a valuable reference for the structural design of micro wind generator blades.

2. Experimental and Method

2.1 Blade Design and Manufacture

Micro- wind power generation represents a sustainable and environmentally friendly approach to energy harvesting. The blades utilized in these systems are fabricated from eco-friendly materials, aligning with design objectives. In this study, PLA was selected as the blade material (Miranda et al., 2022; Suresh et al., 2024). PLA, derived from starch-based plant resources through fermentation and subsequent polymerization, is biodegradable and can decompose entirely into water, carbon dioxide, and organic matter under appropriate conditions, thereby ensuring environmental safety. Additionally, FDM technology was employed to 3D print the designed blades (Zawadzki et al., 2020; Ramírez-Elías et al., 2022). This technique facilitates the rapid production and is particularly effective for the efficient printing of PLA materials, producing no additional waste, and ensuring full utilization of raw materials.

To enhance manufacturing efficiency, the blade structure was simplified by omitting the twist deformation angle design. Additionally, to mitigate auxiliary forces and vibrations caused by deformation at the blade tips, a circular ring structure was employed to reinforce the blade perimeter (Leung et al., 2011). Based on preliminary experimental results, the blade thickness was set at 12 mm, and the *BD* was selected within the range of 103 mm to 127 mm to accommodate installation and testing. The *BA* was chosen within the range of 35° to 55° to eliminate the necessity for additional support structures during 3D printing, thereby preventing material waste. The *BN* was established between 3 and 7; an excessive number may obstruct the windward surfaces of adjacent blades, thereby diminishing overall rotational efficiency. The *BRA* was set within the range of 0° to 1.2°to enhance rotational stability. The blade design adhered to the principle of uniform wall thickness, with the wall thickness maintained at 1.2 mm to reduce weight and ensure high-quality 3D printing performance. The structural parameters and their ranges are summarized in Table 1.

Table 1 Blade parameters and their ranges

Parameters	Unit	Range of value
The blade diameter (BD)	mm	103-127
The blade inclination angle (BA)	°	35-55
The blade number (BN)	No.	3-7
The blade root draft angle (BRA)	°	0-1.2

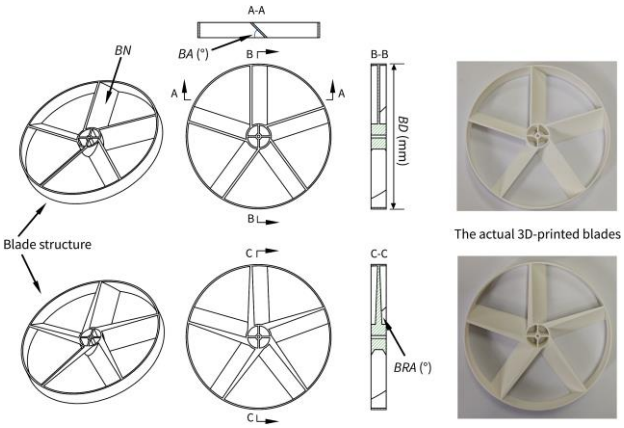

Fig. 1 Blade structural parameters and the actual 3D-printed blades

Figure 1 depicts the blade structure and relevant parameters designed in this study. The blade printing material employed is Bambu PLA Matte, produced by Bambu Lab, characterized by a white color and a material density of 1.31 g/cm³. The 3D printing was executed using the FDM printer P1P manufactured by Bambu Lab, featuring a build volume of 256 × 256 × 256 mm³. Printing parameters were maintained at default settings: a printing temperature of 220°C, a build plate temperature of 65°C, and a printing speed of 200 mm/s. Upon completion of printing, the blades were cooled to room temperature and subsequently removed from the metal PEI plate. After printing, all blades were placed in consistent environment and allowed to stabilize for 24 hours prior to subsequent experimental testing.

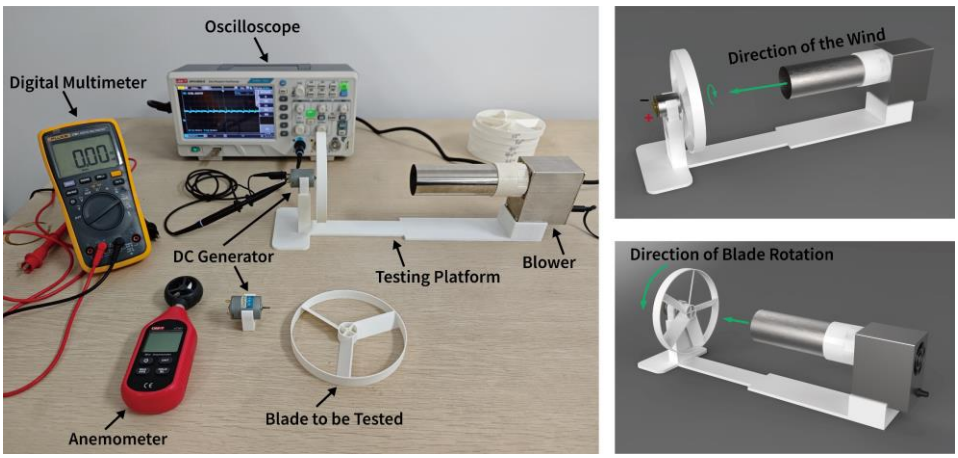

Fig. 2 Composition of the experimental device

2.2 Experimental Setup and Procedure

Blade weight was measured using an electronic balance (Model YT3204, Youkowit Co., Ltd. China) with an accuracy of 0.1 mg. Following weight measurement, experimental tests were conducted. The experimental setup is illustrated in Fig. 2. A small blower (Model A60S) was employed to provide a stable airflow output, with a wind duct diameter of 40 mm. The blower was positioned on the right side of the testing platform, while a small DC generator (Zhuoye Motor Co., Ltd. China) was mounted on the left side to generate electricity through blade rotation. The blades under examination were affixed to the shaft of the DC generator, ensuring alignment between the generator shaft and the blower centerline. The blower knob was adjusted to its maximum setting, and an anemometer (Model UT363, Uni-Trend Technology (China) Co., Ltd.) was positioned at the blower outlet to measure wind speed, recorded at 15 ± 0.2 m/s. During the experiments, a FLUKE digital multimeter (Model 17B+) was connected to the generator output to measure output current, while an oscilloscope (Model UPO1202S-E, Uni-Trend Technology (China) Co., Ltd.) was used to determine the generator's output voltage. All experiments were conducted indoors under windless conditions.

2.3 Single Factor Experiment and Parameter Level Design

Single-factor variation experiments were conducted on selected blade structural features. This method allows for the investigation of the independent effect of each parameter on the target result. When the number of variables is limited and the experimental scale is manageable, single-factor experiments facilitate a clearer identification of the direct relationship between each structural feature and performance, providing a robust basis for future multifactor interaction studies. Although orthogonal experimental design is a powerful tool for analyzing multifactor interactions efficiently, it was not adopted in this study due to the exploratory nature of the investigation and the limited number of design variables. The primary objective was to gain a fundamental understanding of the individual influence of each parameter before moving on to more complex multifactor analyses. The experiments were categorized into four groups according to the type of varying factor, with each group comprising five blades, as presented in Table 2.

Table 2 Grouping of single-factor blade structures

No.	*BD* (mm)	*BA* (°)	*BN*	*BRA* (°)
1	103-127	45	5	0
2	115	35-55	5	0
3	115	45	3-7	0
4	115	45	5	0-1.2

Figure 3(a) illustrates the influence of *BD* on generator output current (C_g), output voltage (V_g), and blade weight (W_b). The results indicate that as *BD* increases, C_g exhibits a slight decreasing trend, with a maximum variation of 8.27%. In contrast, V_g decreases significantly with increasing *BD*, reaching a variation of 32.84%. Meanwhile, Wb gradually increases with *BD*, with a variation of 21.47%. Figure 3(b) presents the effect of *BA* on the three target metrics. As *BA* increases, all three metrics show a decreasing trend, with C_g, V_g, and W_b decreasing by 51.54%, 52.05%, and 12.53%, respectively. Figure 3(c) displays the impact of *BN* on the target metrics. The findings indicate that as *BN* increases, all three metrics exhibit an increasing trend. Specifically, C_g increases by 286.57%, V_g by 128.57%, and W_b by 42.09%. Figure 3(d) shows the effect of *BRA* on the target metrics. It is evident that C_g and V_g remain relatively stable with changes in *BRA*, while W_b increases as *BRA* becomes larger.

The single-factor experiments reveal that *BD*, *BN*, and *BA* significantly influence C_g, V_g, and W_b, while changes in *BRA* do not notably affect the generator's power output. Therefore, *BRA* was excluded from further analysis. The final design parameters and their levels are summarized in Table 3.

Table 3 Parameters design and levels

Parameters	Level		
	-1	0	1
BD (mm)	103	115	127
BA (°)	35	45	55
BN	3	5	7

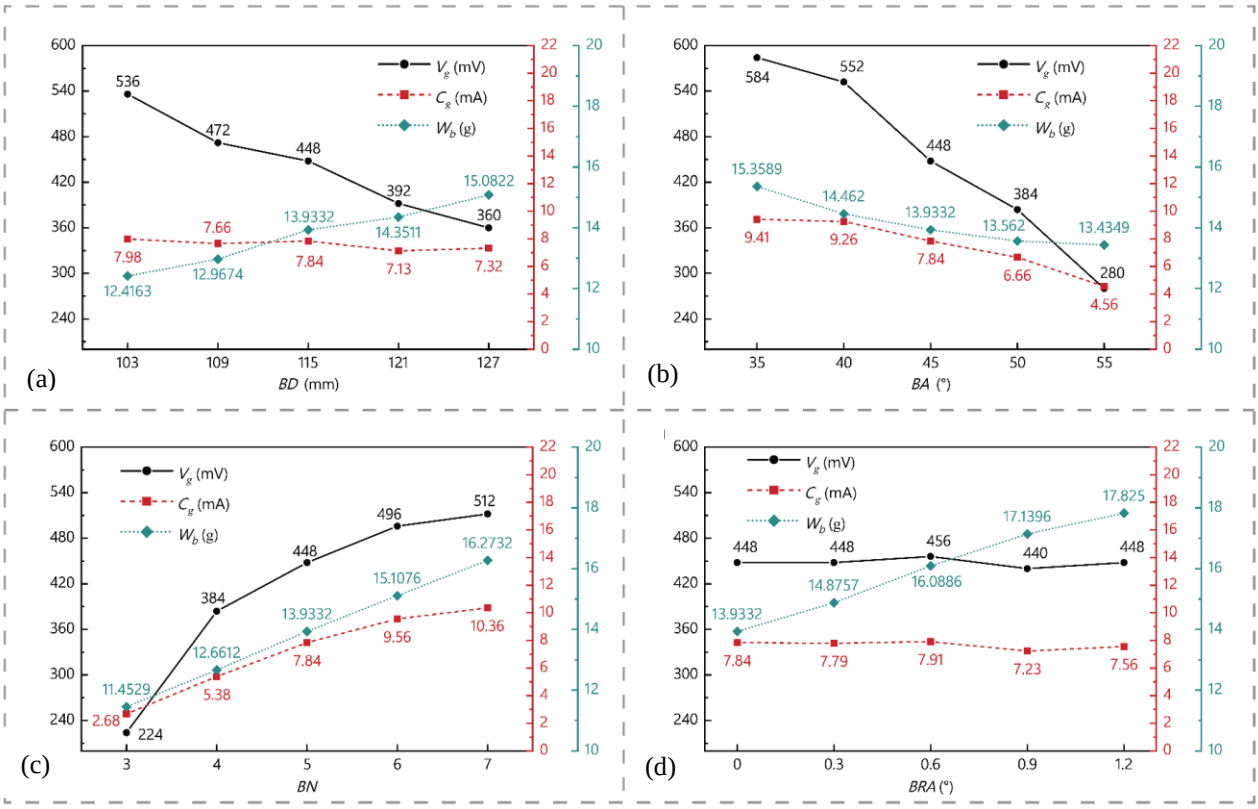

Fig. 3 (a) Effect of *BD* on C_g, V_g and W_b (b) effect of *BA* on C_g, V_g and W_b (c) effect of *BN* on C_g, V_g and W_b (d) effect of *BRA* on C_g, V_g and W_b

2.4 Response Surface Methodology and BBD Experimental Design

Based on the results of single-factor experiments, RSM was employed to further evaluate the effect of each structural parameter on the target values and to explore the interactions between parameters. This experimental design approach is particularly suitable for multivariable problems (Yu et al., 2022), as it enables effective assessment of the individual effects of variables on the target values and their interactions with a relatively small number of experimental runs (Sharma et al., 2023; Zhao et al., 2023; Minhas et al., 2021). RSM employs a second-order polynomial as the fitting function to derive a predictive relationship equation between the variables and the target values (Li et al., 2024; Zhang et al., 2023), as expressed in Eq. (1). The choice of a second-order polynomial is based on its capacity to model both linear and quadratic effects of variables, which is crucial for capturing potential interactions between factors and their non-linear effects. A second-order polynomial strikes a balance between model complexity and the number of experimental runs, making it suitable for capturing key relationships without overfitting the model.

$$Y(X) = \alpha_0 + \sum_{i=1}^{k} \alpha_i X_i + \sum_{i<j}^{k} \sum_{j=2}^{k} \alpha_{ij} X_i X_j + \sum_{i=1}^{k} \alpha_{ii} X_i^2 \quad (1)$$

where $Y(X)$ represents the target response values, X denotes the independent variables (structural parameters), α_0 is the intercept term, α_i represents the first-order coefficients, α_{ij} corresponds to the interaction term coefficients, α_{ii} denotes the quadratic term coefficients, and k is the number of experimental variables.

In response surface experimental design, the central composite design (CCD) and BBD are both widely used methodologies. However, for an equivalent number of variable parameters, BBD requires fewer experimental runs (Yu et al., 2022; Zhao et al., 2023). Therefore, based on the parameters and corresponding levels listed in Table 3, the BBD method was selected to construct the experimental grouping design. The detailed grouping parameters and experimental results are provided in Table 4.

2.5 NSGA-III Optimization Method

In this study, the correlation equations established between each variable and the three target response values using RSM serve as objective functions. The NSGA-III was selected to solve these three functions, with the goal of maximizing the C_g and V_g values while minimizing W_b. As a key algorithm for multi-objective optimization, NSGA-III is particularly suited to high-dimensional problems involving three or more conflicting objectives (Gu et al., 2022; Wang et al., 2023). Its structure is similar to that of NSGA-II, but it introduces well-distributed reference points in the objective space, which improve population diversity and facilitate a more uniform coverage of the Pareto front (Yu et al., 2024). Compared to commonly used methods, NSGA-III demonstrates clear advantages in addressing many-objective scenarios. Traditional algorithms such as Genetic Algorithms (GA) and NSGA-II perform effectively for two objectives but

Table 4 BBD experimental design and test data

Std	Run	*BD* (mm)	*BA* (°)	*BN*	C_g (mA)	W_b (g)	V_g (mV)
7	1	-1	0	1	11.47	14.3678	600
3	2	-1	1	0	5.18	12.0779	368
2	3	1	-1	0	8.98	16.9263	480
5	4	-1	0	-1	2.64	10.3596	264
1	5	-1	-1	0	10.13	13.6235	688
6	6	1	0	-1	2.59	12.5674	176
17	7	0	0	0	7.64	13.7345	432
12	8	0	1	1	7.98	15.6952	360
11	9	0	-1	1	11.92	18.2286	592
16	10	0	0	0	7.66	13.8558	440
10	11	0	1	-1	1.03	11.2758	80
9	12	0	-1	-1	4.18	12.3682	400
8	13	1	0	1	10.31	17.8231	432
13	14	0	0	0	7.42	13.8598	424
14	15	0	0	0	7.52	13.8889	432
4	16	1	1	0	4.72	14.8004	240
15	17	0	0	0	7.48	13.9137	440

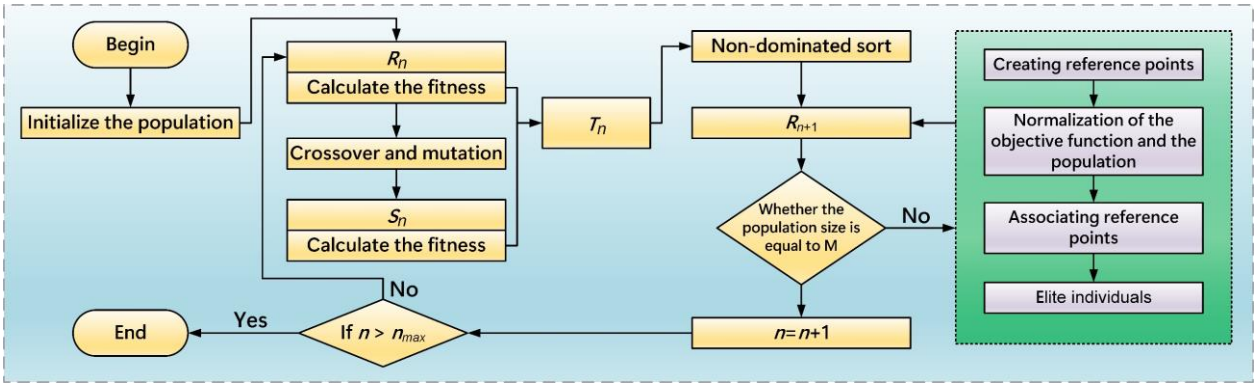

Fig. 4 Flowchart of NSGA-III

typically show reduced diversity and convergence accuracy as the number of objectives increases. Particle Swarm Optimization (PSO), though computationally efficient, is prone to premature convergence and has limited performance in complex, multi-modal design spaces. Sequential quadratic programming (SQP), a gradient-based method, is more applicable to smooth and convex problems, but it frequently becomes trapped in local optima in nonlinear and non-convex contexts, such as those described by RSM equations with interaction terms.

NSGA-III, as an evolutionary algorithm, demonstrates strong robustness in exploring complex, nonlinear, and non-convex design spaces while maintaining both diversity and convergence. Its effectiveness has been widely validated across various engineering design applications. Therefore, NSGA-III was chosen as the optimization framework in this study to enable a comprehensive exploration of trade-offs among mechanical and electrical performance objectives and to yield a well-distributed set of high-quality Pareto-optimal solutions.

Figure 4 outlines the NSGA-III optimization process. The process begins with the random generation of an initial population R_0 of size M, following the specified objective function directions and variable bounds. The fitness of each individual in population R_n is evaluated, and an offspring population S_0 is generated via crossover and mutation. The fitness of the offspring is then calculated. The original population R_n and offspring population S_n are merged to form a composite population T_n (with n representing the generation number), which is subjected to non-dominated sorting. Non-dominated layers are successively included in the next-generation population R_{n+1} until its size reaches M. If the size does not exactly equal M, reference points are generated in the objective space, and both objective functions and the population are normalized into this space. The distance between each individual and the reference points is determined, and the closest reference point is identified. Elite individuals are selected from each layer and added to R_{n+1} to reach the target population size M. This approach maintains solution diversity and convergence throughout the objective space.

In this study, higher generator output current and voltage represent improved blade rotational performance, necessitating the maximization of C_g and V_g. At the same time, W_b is minimized to reduce material use under these operational conditions. According to the predictive

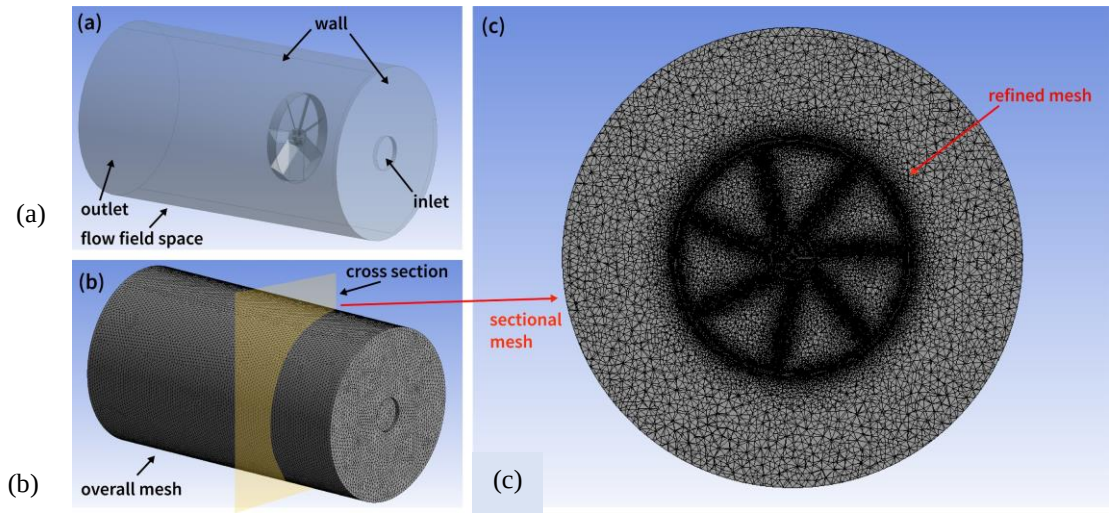

Fig. 5 (a) Flow field space (b) the overall mesh (c) the sectional mesh

model established by RSM and practical design requirements, the optimized multi-objective equation model is formulated as shown in Eq. (2) and Eq. (3).

$$\begin{cases} f_1 = C_g(BD, BA, BN) \rightarrow \text{Maximize} \\ f_2 = W_b(BD, BA, BN) \rightarrow \text{Minimize} \\ f_3 = V_g(BD, BA, BN) \rightarrow \text{Maximize} \end{cases} \tag{2}$$

$$\begin{cases} BD \in [103,127] \\ BA \in [35,55] \\ BN \in [3,7] \end{cases} \tag{3}$$

No additional nonlinear constraints are imposed. The design variable bounds are determined based on preliminary experimental results, manufacturability, and additive manufacturing limitations. The objective functions are derived from the second-order polynomial equations developed via RSM, and the NSGA-III algorithm is applied to identify Pareto-optimal solutions within the defined design space.

2.6 CFD Simulation Method

To further examine the experimental findings, computational fluid dynamics (CFD) simulation was conducted. From an aerodynamic perspective, the effects of changes in structural parameters on blade surface pressure and turbulence intensity were assessed, providing an indirect explanation for their influence on power generation performance. Generally, an increase in wind pressure on the blade surface results in a higher rotational speed of the blade, which subsequently enhances the electromagnetic induction in the generator, leading to increased output voltage and current.

As depicted in Fig. 5(a), the computational domain was defined as a flow field space with a diameter of 200 mm and a length of 355 mm. Blades were aligned along the axis and positioned 112.5 mm from the velocity inlet, consistent with the experimental configuration. To balance computational efficiency and accuracy, the overall flow field mesh size was set at 4mm, with a refined mesh size of 0.6 mm near the blades. Tetrahedral meshing was used for the domain. The resulting overall and sectional meshes are shown in Figs. 5(b) and 5(c). A transient simulation was performed using the standard k-epsilon turbulence model with enhanced wall treatment, allowing accurate resolution of the boundary layer for a wide range of near-wall y+ values. In this study, the y+ values near the blade surfaces were controlled between 1 and 25, aligning with the requirements of the turbulence model and wall treatment. The inlet wind speed was set at 15 m/s. A six-degree-of-freedom (6-DOF) dynamic mesh was applied, using the measured blade mass. The blade's center of mass and moment of inertia were determined via 3D modeling software. The simulation employed 200 time steps, with a time step size of 0.001 s. Following the calculations, data regarding blade surface pressure distribution, static and dynamic pressure on the blade's mid-plane, and turbulence intensity were extracted.

3. Result and Discussion

3.1 ANOVA for RSM and Fitting Formula

The ANOVA results obtained from RSM enable effective evaluation of the effect of various factors on the target values, with p-value and F-value serving as key indicators. The p-value denotes the probability of rejecting the null hypothesis. A smaller p-value indicates greater statistical significance of the model. Specifically, a p-value below 0.05 suggests statistical significance, whereas a p-value below 0.0001 indicates high significance and reflects a high degree of accuracy or reliability (Maleki et al., 2021). The F-value, calculated as the ratio of the mean square between groups to the mean square within groups, assesses whether changes in the independent variables account for significant variation in the target values. A larger F-value demonstrates that variation between groups substantially exceeds that within groups, indicating a significant effect of the independent variables on the target values.

In the statistical analysis of RSM, C.V. % quantifies the model's prediction error as a percentage of the mean response values. A lower C.V. % indicates enhanced model stability, with a widely accepted threshold of less

Table 5 Quadratic model ANOVA for C_g

Source	Sum of Squares	df	Mean Square	F-value	p-value	
Model	7.38	9	0.8205	966.14	< 0.0001	significant
BD	0.0289	1	0.0289	34.02	0.0006	
BA	1.43	1	1.43	1689.73	< 0.0001	
BN	5.41	1	5.41	6375.89	< 0.0001	
(*BD*×*BA*)	0.0017	1	0.0017	2.01	0.1989	
(*BD*×*BN*)	0.0064	1	0.0064	7.57	0.0284	
(*BA*×*BN*)	0.0404	1	0.0404	47.57	0.0002	
$(BD)^2$	0.0012	1	0.0012	1.45	0.2683	
$(BA)^2$	0.0479	1	0.0479	56.42	0.0001	
$(BN)^2$	0.3935	1	0.3935	463.36	< 0.0001	
C.V. %	1.14		Predicted R^2	0.9899		
Adjusted R^2	0.9982		Adeq Precision	111.5155		

Table 6 Quadratic model ANOVA for W_b

Source	Sum of Squares	df	Mean Square	F-value	p-value	
Model	1.29	9	0.1437	501.79	< 0.0001	significant
BD	0.3013	1	0.3013	1051.99	< 0.0001	
BA	0.1127	1	0.1127	393.33	< 0.0001	
BN	0.8482	1	0.8482	2961.28	< 0.0001	
(*BD*×*BA*)	0.0007	1	0.0007	2.3	0.173	
(*BD*×*BN*)	0.0027	1	0.0027	9.59	0.0174	
(*BA*×*BN*)	0.0055	1	0.0055	19.35	0.0032	
$(BD)^2$	0.0005	1	0.0005	1.82	0.2196	
$(BA)^2$	0.0215	1	0.0215	74.94	< 0.0001	
$(BN)^2$	0.0011	1	0.0011	4.01	0.0852	
C.V. %	0.4523		Predicted R^2	0.9791		
Adjusted R^2	0.9965		Adeq Precision	81.4702		

Table 7 Quadratic model ANOVA for V_g

Source	Sum of Squares	df	Mean Square	F-value	p-value	
Model	285.41	9	31.71	134.08	< 0.0001	significant
BD	27.03	1	27.03	114.26	< 0.0001	
BA	111.58	1	111.58	471.73	< 0.0001	
BN	113.44	1	113.44	479.62	< 0.0001	
(*BD*×*BA*)	0.0991	1	0.0991	0.4188	0.5382	
(*BD*×*BN*)	0.1328	1	0.1328	0.5613	0.4782	
(*BA*×*BN*)	8.12	1	8.12	34.32	0.0006	
$(BD)^2$	0.2816	1	0.2816	1.19	0.3114	
$(BA)^2$	0.6006	1	0.6006	2.54	0.1551	
$(BN)^2$	23.9	1	23.9	101.06	< 0.0001	
C.V. %	2.48		Predicted R^2	0.9129		
Adjusted R^2	0.9868		Adeq Precision	46.3694		

than 10%. The Predicted R^2 assesses the model's capacity to predict new data not used in model fitting; values approaching 1 signify superior predictive performance. The Adjusted R^2 reflects the model's fit for the current dataset, with higher values indicating stronger explanatory power and improved fit. It is advisable that the difference between Predicted R^2 and Adjusted R^2 remains below 0.2 to ensure alignment between the model's predictive and fitting capabilities. Adequate Precision (Adeq Precision), which evaluates the ratio of the model's signal to noise, should exceed 4 to confirm that the signal is significantly stronger than the noise, thus ensuring effective predictive performance.

Tables 5, 6, and 7 provide the ANOVA results for the quadratic models of C_g, W_b, and V_g , respectively. The p-values for all three models are less than 0.0001, demonstrating high significance. The variables *BN*, *BA*, and *BD* emerge as significant factors across all models. Based on the F-value, the order of influence for C_g and V_g is *BN* > *BA* > *BD*, while for W_b, it is *BN* > *BD*> *BA*. Regarding interaction terms, the order of influence on C_g, W_b, and V_g is consistently (*BA* × *BN*) > (*BD* × *BN*) > (*BD* × *BA*). The statistical results in Tables 4, 5, and 6 show C.V. % values of 1.14, 0.4523, and 2.48, respectively. The Predicted R^2 values are all close to 1, and the differences between Predicted R^2 and Adjusted R^2 are all less than 0.2,

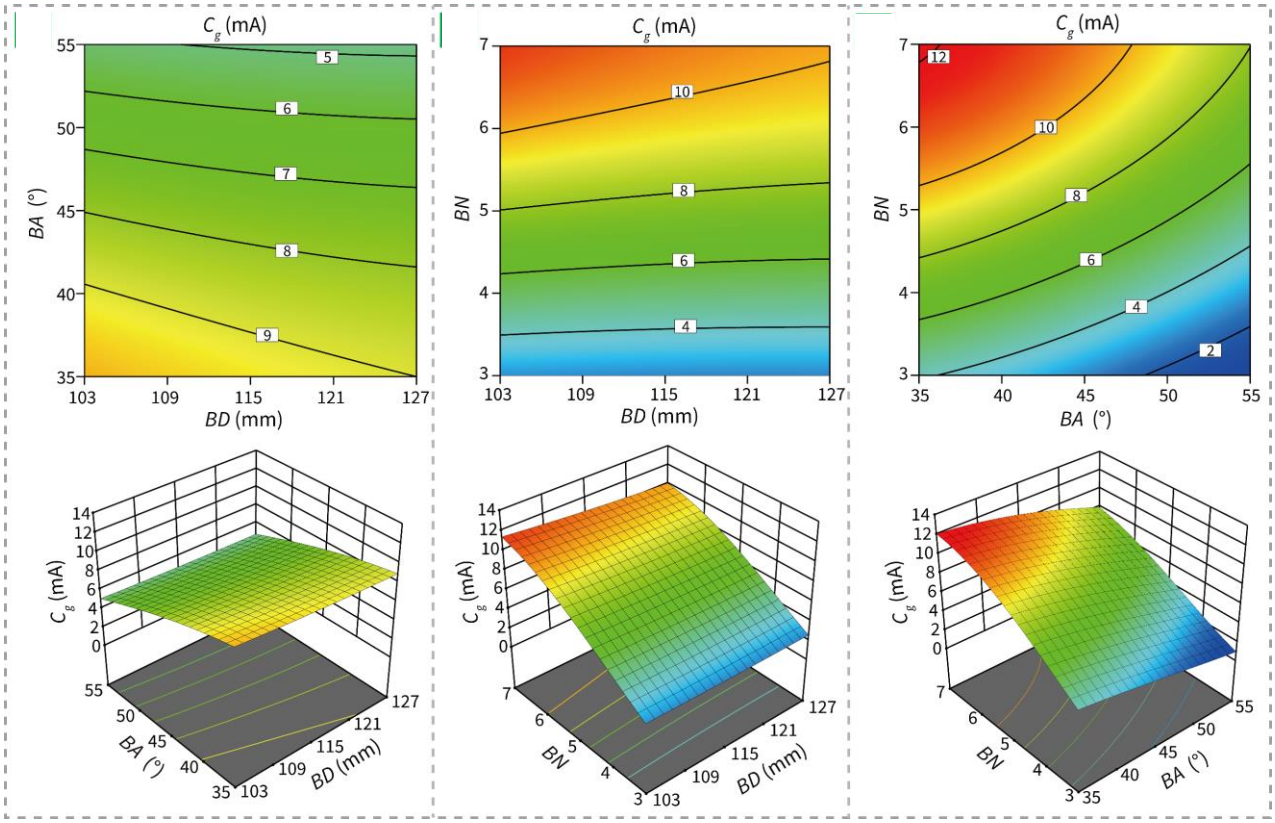

(a) (b) (c)

Fig. 6 (a) Effect of *BD* and *BA* on C_g (b) effect of *BD* and *BN* on C_g (c) effect of *BA* and *BN* on C_g

confirming the models' consistency and reliability. The Adeq Precision values are 111.5155, 81.4702, and 46.3694 for C_g, W_b, and V_g, respectively, indicating robust signal-to-noise ratios and strong predictive capabilities. These results affirm that the models exhibit a good fit and reliable predictive performance. The corresponding quadratic regression equations for predicting C_g, W_b, and V_g are presented in Eqs. (4), (5), and (6).

$$C_g = (1.73079 - 0.031684 \times BD + 0.008717 \times BA + 1.1416 \times BN + 0.000172 \times BD \times BA - 0.00167 \times BD \times BN + 0.005025 \times BA \times BN + 0.000119 \times (BD)^2 - 0.001067 \times (BA)^2 - 0.076426 \times (BN)^2)^2 \quad (4)$$

$$W_b = (1.55856 + 0.033289 \times BD - 0.05452 \times BA + 0.162282 \times BN - 0.00011 \times BD \times BA + 0.001092 \times BD \times BN - 0.00186 \times BA \times BN - 7.7e^{-5} \times (BD)^2 + 0.000714 \times (BA)^2 - 0.00413 \times (BN)^2)^2 \quad (5)$$

$$V_g = (65.48623 - 0.58726 \times BD - 0.5405 \times BA + 5.50705 \times BN + 0.001311 \times BD \times BA - 0.00759 \times BD \times BN + 0.071229 \times BA \times BN + 0.001796 \times (BD)^2 - 0.00378 \times (BA)^2 - 0.59566 \times (BN)^2)^2 \quad (6)$$

3.2 Interactive Effects of Structural Parameters on Generator Output Current and Output Voltage

Figure 6 illustrates the contour plots and corresponding 3D diagrams depicting the interactive effects of three structural parameters on C_g. In Fig. 6(a), with *BN* fixed at 5 and *BA* constant, C_g decreases slowly as *BD* increases. However, an increase in *BA* significantly reduces C_g, largely unaffected by variations in *BD*. Figure 6 (b) shows that when *BA* is set at 45° and *BN* is constant, *BD* minimally influences C_g, while an increase in *BN* leads to a notable rise in C_g. According to Fig. 6 (c), when *BD* is set to 115 mm, C_g decreases as *BA* increases. However, this reduction is limited when *BN* remains constant, whereas an increase in *BN* effectively enhances C_g, particularly at smaller *BA* values.

Figure 7 demonstrates the interactive effects of the three structural parameters on V_g. As indicated in Fig. 7(a), when *BN* is fixed at 5, V_g increases as both *BA* and *BD* decrease. Conversely, increases in either *BA* or *BD* result in a reduction in V_g. From Fig. 7(b), it is evident that when *BA* is set at 45°, V_g achieves relatively higher values when *BD* is less than 115 mm and *BN* exceeds 5. According to Fig. 7(c), when *BD* is fixed at 115 mm, V_g exceeds 500 mV under conditions where *BA* is less than 45° and *BN* is greater than 4.

The rationale for the aforementioned results is that under fixed experimental conditions, the outlet diameter remains constant. The independent increase in *BD* does not significantly enlarge the core region of wind load on the blade, as illustrated in Figs. 8 and 9. Furthermore, a comparison of the CFD simulation results for the BBD experimental group (Table 4), specifically between run-1 and run-13 as well as run-2 and run-16—where the blade parameters are identical except for diameter—reveals consistent distributions of static pressure, dynamic pressure, and turbulence intensity across the center planes of the blades within each pair, as shown in Figs. 10(a), 10(e), 10(b), and 10(f). This consistency suggests that the

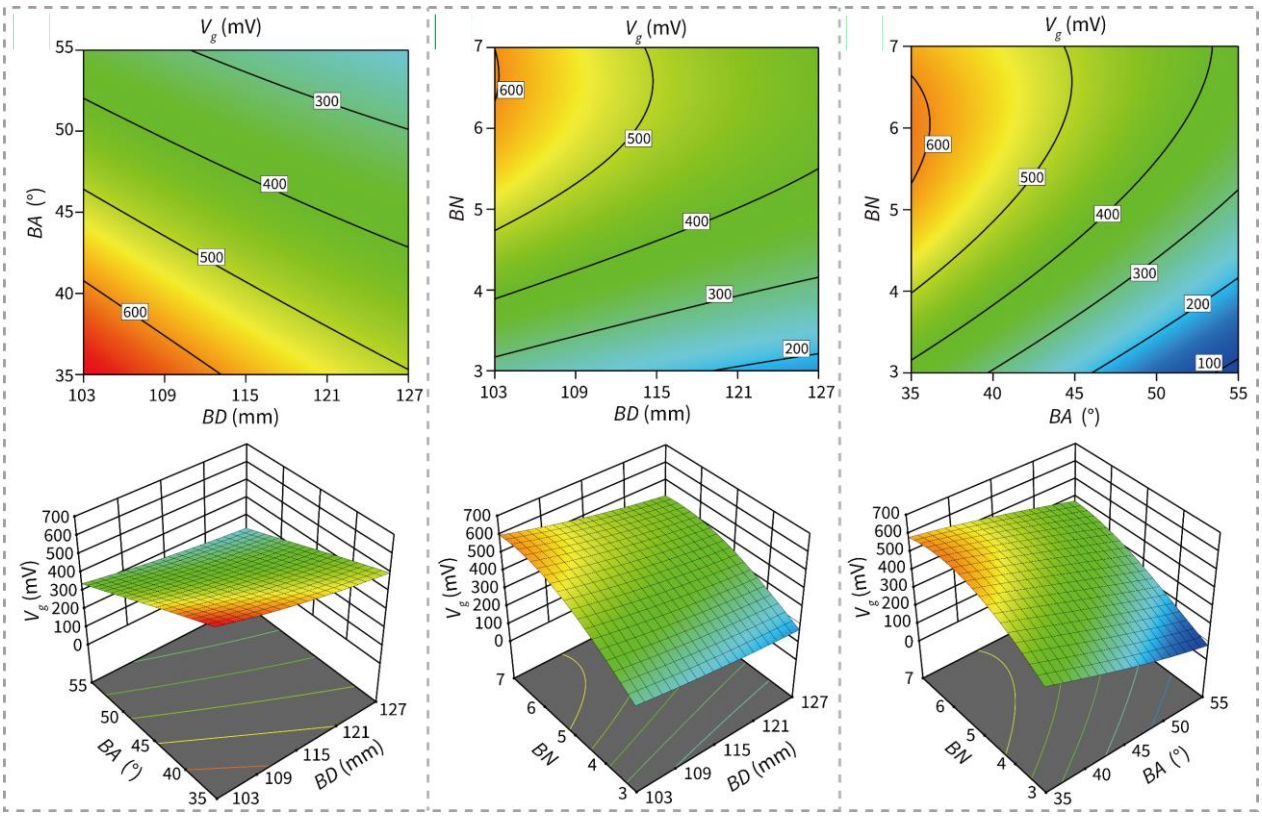

(a) (b) (c)

Fig. 7 (a) Effect of *BD* and *BA* on V_g (b) effect of *BD* and *BN* on V_g (c) effect of *BA* and *BN* on V_g

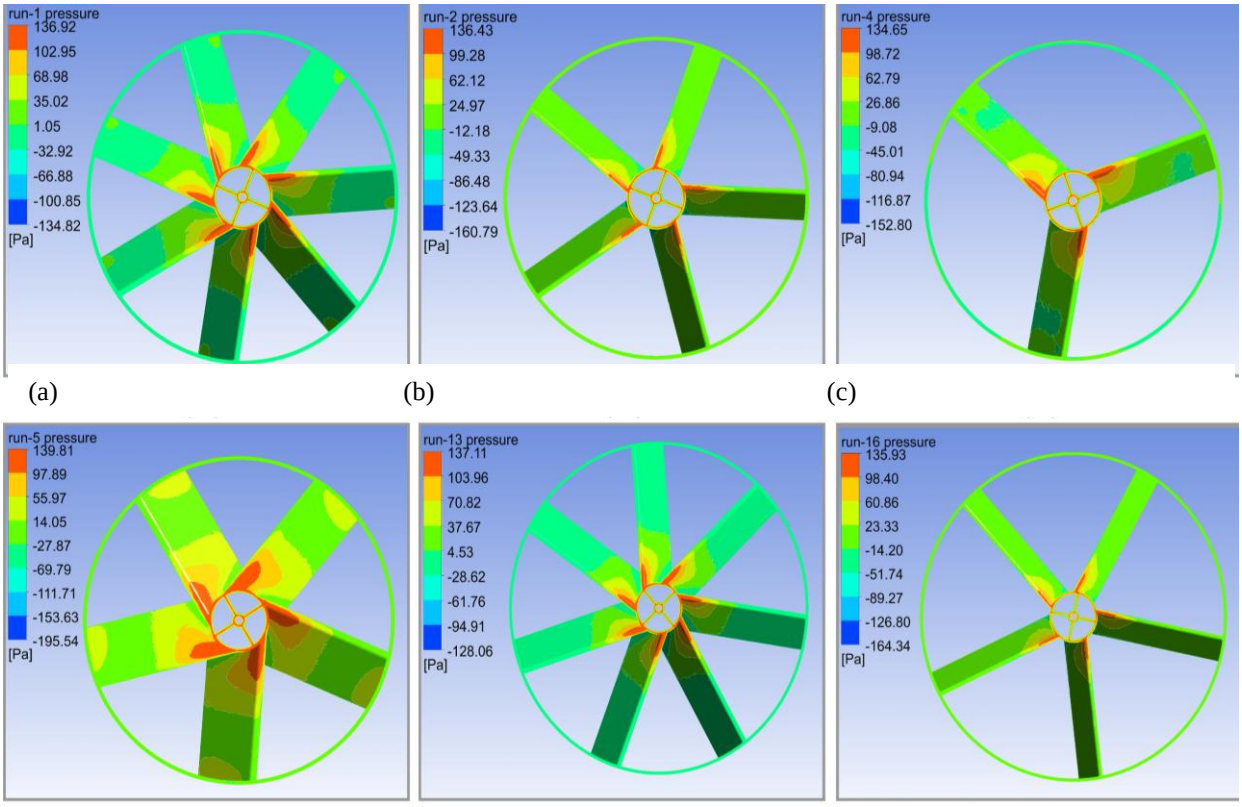

(a) (b) (c)

(d) (e) (f)

Fig. 8 Blade pressure of the BBD experimental group: (a) run-1 (b) run-2 (c) run-4 (d) run-5 (e) run-13 (f) run-16

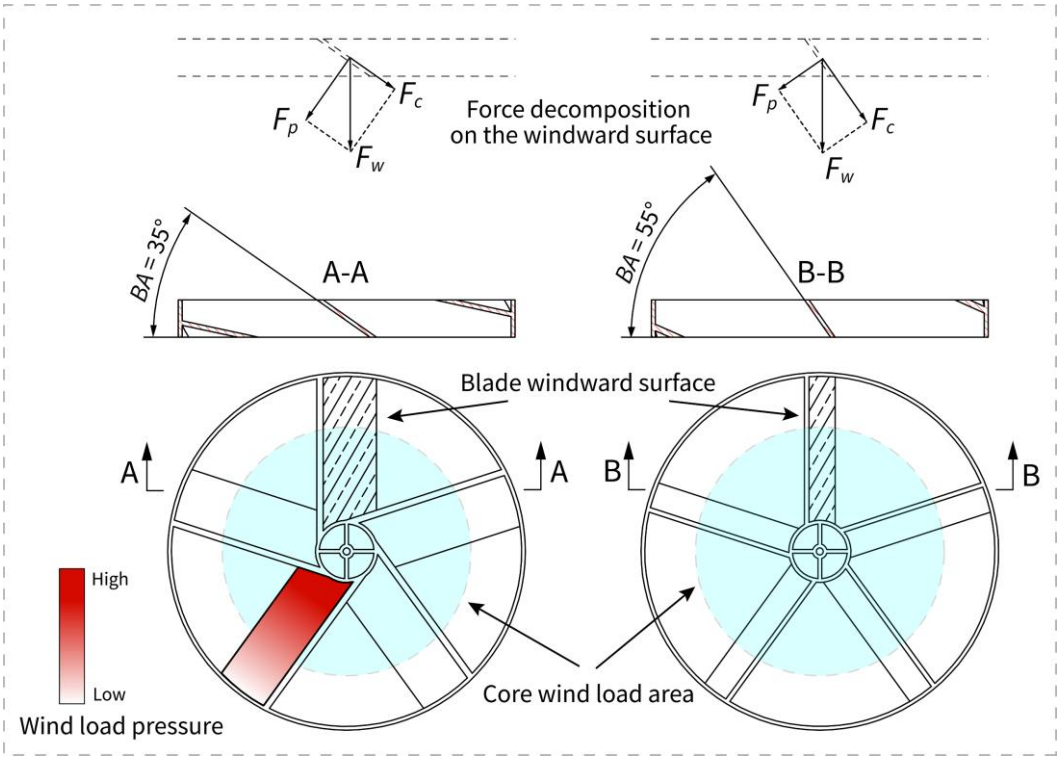

Fig. 9 Schematic of blade wind load area and the force condition of the blades

aerodynamic forces acting on each blade within the respective pairs remain unchanged during airflow passage, with the key difference being the increase in *BD*, resulting in greater weight. Therefore, with the same applied force, moving a heavier object becomes more challenging, leading to superior experimental performance in run-1 compared to run-13, and similarly, in run-2 over run-16. Additionally, the reduction in C_g due to the increased diameter is less pronounced than that in V_g, as the aerodynamic forces on the blades remain similar. An increase in *BD* directly lowers the generator's output voltage. Meanwhile, the increased blade weight raises the load on the generator, thereby enhancing rotational stability, which aids in maintaining the output current. Therefore, the overall variation remains relatively minor.

When the *BD* and *BA* are held constant, a comparison between run-1 and run-4 shows that, as illustrated in Figs. 8(a) and 8(c), an increase in the *BN* directly expands the overall surface area subjected to aerodynamic forces. This, in turn, indirectly increases the driving force for blade rotation, resulting in higher C_g and V_g. Furthermore, as shown in Figs. 10(a) and 10(c), increasing the *BN* broadens the distribution area of both static and dynamic pressure on the blades, while the turbulence intensity region becomes more uniform. This indicates enhanced stability in blade rotation.

3.3 Interactive Effects of Structural Parameters on Blade Weight

The interactive effects of *BD*, *BA*, and *BN* on W_b are depicted in Fig. 11. As illustrated in Fig. 11(a), when *BN* is fixed at 5, W_b increases with *BD* but decreases with *BA*, although the influence of *BA* is less significant than that of *BD*. In Fig. 11(b), when *BA* is set at 45°, W_b increases with both *BN* and *BD*; however, when *BN* is held constant, *BD* exerts a limited effect on W_b. From Fig. 11(c), it can be observed that when *BD* is fixed at 115 mm, W_b increases with *BN*, while the impact of *BA* on W_b remains minimal. The primary reason for these trends is that increasing *BD*, increasing *BN*, and reducing *BA* directly lead to an increase in blade volume, which subsequently raises blade weight. Among these factors, under the current experimental conditions, changes in *BN* have the most pronounced impact on blade volume, followed by *BD*, while changes in *BA* contribute relatively little to the variation in blade volume.

3.4 Optimization Results of NSGA-III and Comparison of Experimental Tests

To comprehensively cover the target space, reduce the risk of converging on local optima, and ensure computational efficiency, reference points were set to 20, the maximum number of iterations to 100, and the population size to 200. Additionally, to enhance the population's search capability and maintain diversity, the crossover probability was established at 0.7, the mutation participation rate at 0.4, and the mutation rate at 0.02.

Figure 12 presents the Pareto front solutions derived from iterative calculations. Based on the objective conditions, solutions were prioritized according to the criteria where V_g exceeds 720 mV, C_g exceeds 12 mA, and W_b is less than 15 g. Two sets of optimized data were generated, as displayed in Table 8. In both sets, the *BD* value is 103 mm, and the *BN* must be an integer, selected as 6. The *BA* values exhibit minor differences, recorded as 35.92° and 35.42°, respectively. Utilizing the optimized structural parameters, the three-dimensional models of the blade were refined and 3D printed. Experimental tests

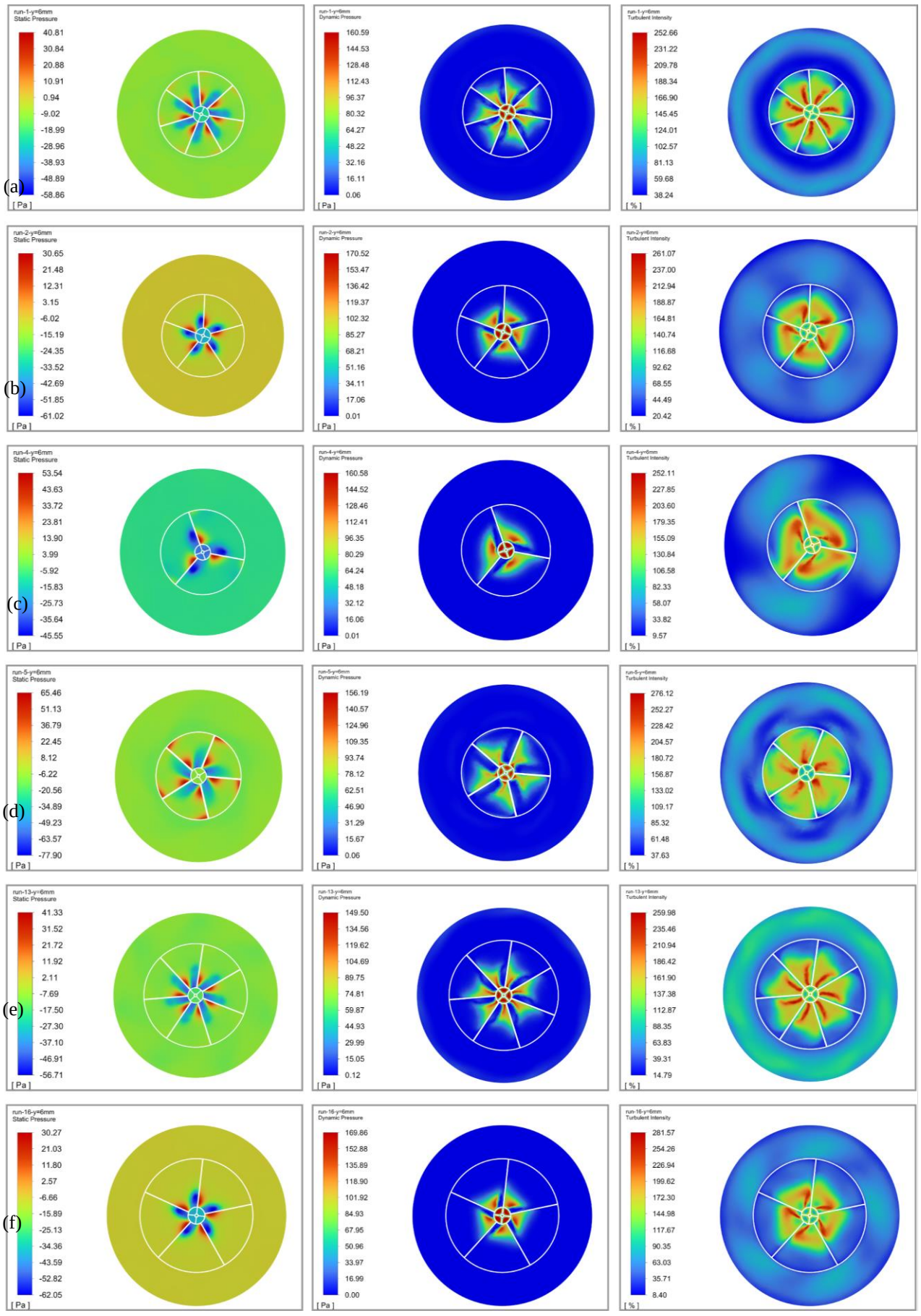

Fig. 10 Static pressure, dynamic pressure and turbulence intensity of the blade in the BBD experimental group: (a) run-1 (b) run-2 (c) run-4 (d) run-5 (e) run-13 (f) run-16

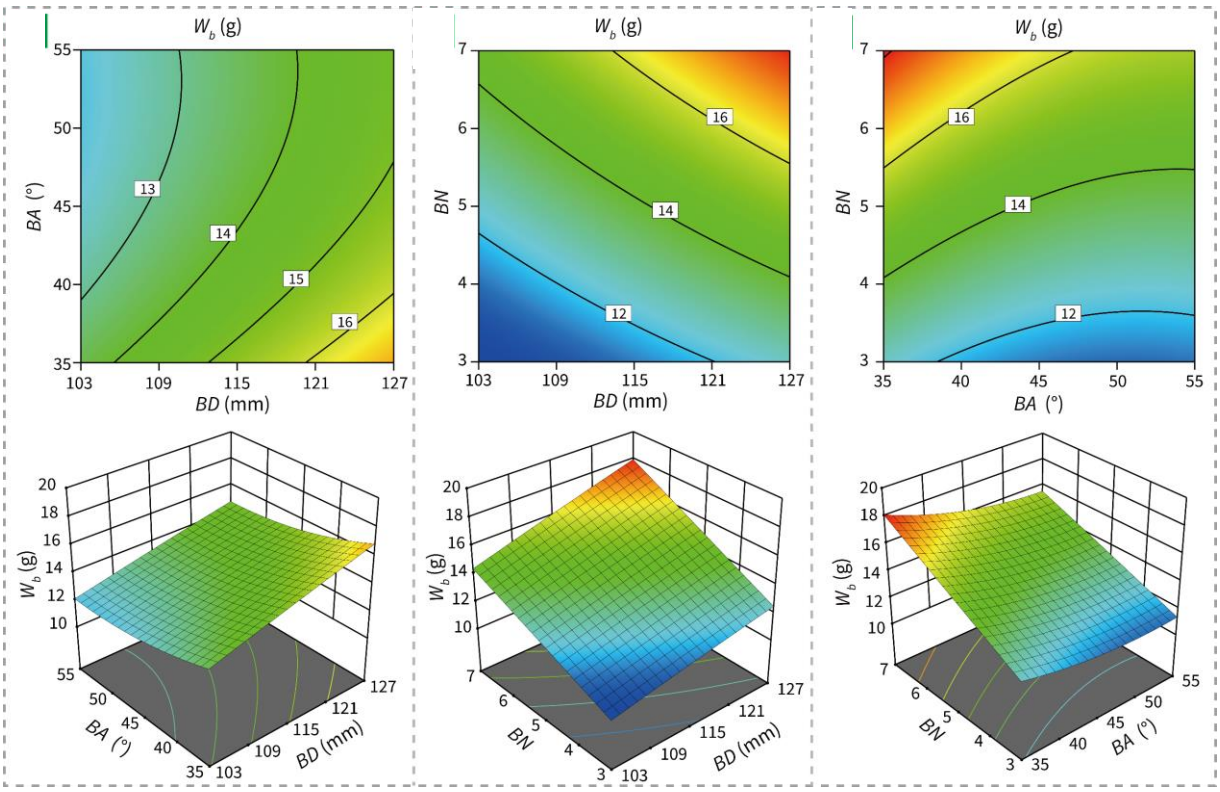

Fig. 11 (a) Effect of *BD* and *BA* on W_b (b) effect of *BD* and *BN* on W_b (c) effect of *BA* and *BN* on W_b

Table 8 Comparison between the optimized predicted data and actual test data

S.no.	*BD* (mm)	*BA* (°)	*BN*	C_g (mA)	W_b (g)	V_g (mV)
Optimization 1	103.0001	35.9187	6.2360	12.2677	14.9191	721.9479
Optimization 2	103.0005	35.4249	6.1503	12.2106	14.9159	728.6831
Experimental test 1	103	35.92	6	11.95	14.6152	720
Experimental test 2	103	35.42	6	11.78	14.8219	720
Error 1				2.59%	2.04%	0.27%
Error 2				3.53%	0.63%	1.19%

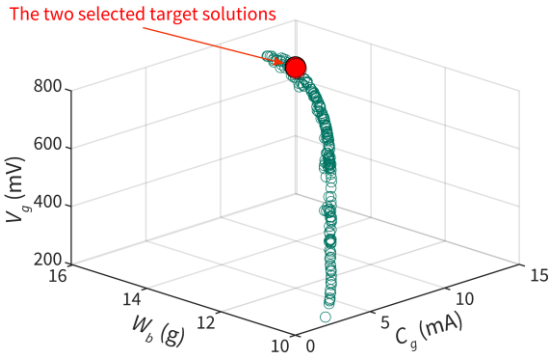

Fig. 12 Pareto front solution set for multi-objective optimization and the selected target solutions

were subsequently performed, comparing the calculated target results with the actual test results. In the first set, the errors in the C_g and V_g values were smaller than in the second set, although the current value was somewhat higher. For W_b, the error in the second set was smaller than in the first set; however, the blade weight in the first set was lighter. Therefore, the final selected optimized structural parameters were: *BD* = 105 mm, *BA* = 35.92°,

Table 9 Optimized parameters and RSM experimental parameters

No.	*BD* (mm)	*BA* (°)	*BN*
Optimization	103	35.92	6
Run-5	103	35	5
Run-9	115	35	7
Run-4	103	45	3

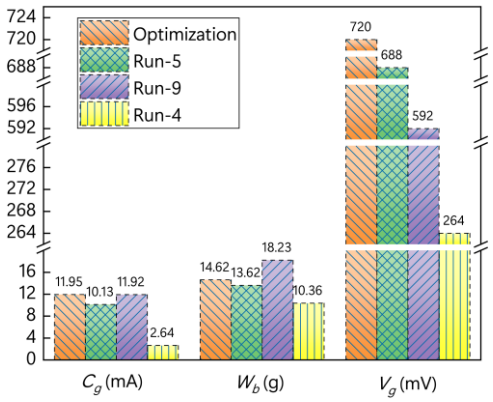

Fig. 13 Comparison of the optimized results with RSM experimental groups

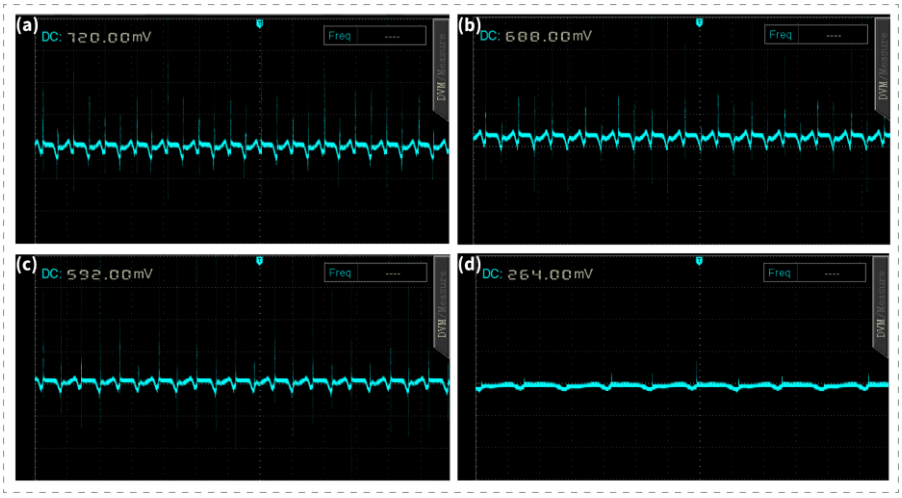

Fig. 14 (a) Optimized Vg value (b) run-5 Vg value (c) run-9 Vg value (d) run-4 Vg value

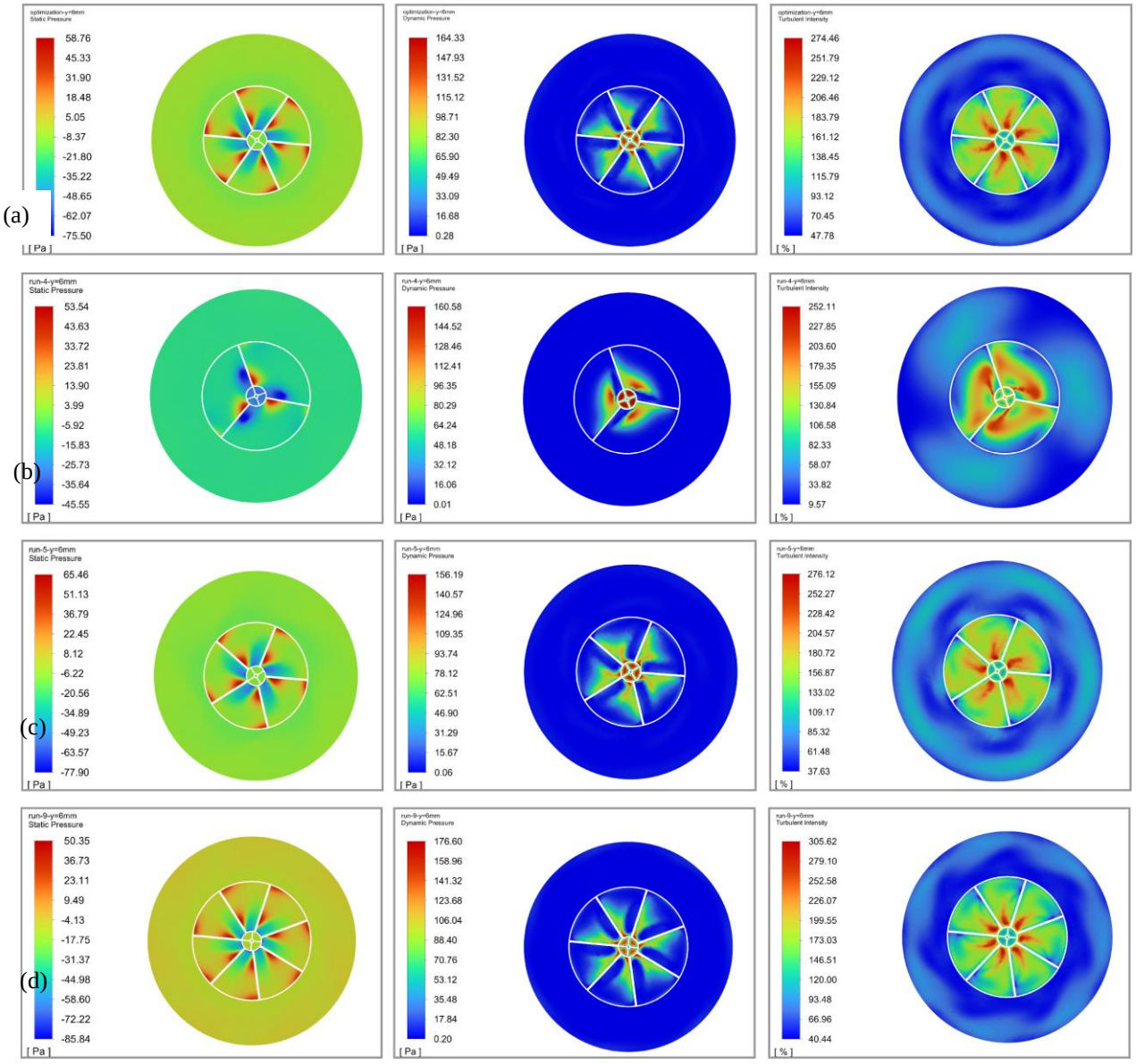

Fig. 15 Static pressure, dynamic pressure and turbulence intensity of the blade: (a) optimization (b) run-4 (c) run-5 (d) run-9

and *BN* = 6. The experimental target results obtained were: output current 11.95 mA, output voltage 720 mV, and blade weight 14.6152 g.

The optimized blade was compared with those from run-4, run-5, and run-9. The structural parameters of each blade are detailed in Table 9, with experimental test results illustrated in Figs. 13 and 14, and simulation results presented in Fig. 15. Compared to run-4, the optimized blade achieved a 352.65% increase in C_g and a 172.73% increase in V_g. Although the blade in run-4 is lighter, the configuration involving the adjustment of the blade tilt angle and reduction in the *BN* significantly compromises rotational performance, as demonstrated in Figs. 15(a) and 15(b). In run-4, the static and dynamic pressure distributions are overly concentrated, and the turbulence intensity distribution is uneven, leading to suboptimal blade rotation performance.

When compared to run-5, the optimized blade resulted in a 17.97% increase in C_g and a 4.65% increase in V_g. Although the blade weight increased by 1 g, this marginal increase remains acceptable. Additionally, as illustrated in Figs. 15(a) and 15(c), the turbulence intensity distribution around the optimized blade is more uniform, forming a ring-like pattern that indicates improved rotational stability.

In comparison to run-9, while maintaining a higher C_g value, the optimized blade achieved a 21.62% increase in V_g and a 19.8% reduction in blade weight. According to Figs. 15(a) and 15(d), the static and dynamic pressure distributions for run-9 and the optimized blade are quite similar; however, the turbulence intensity region around the blade exhibits clustered peak formations, which degrade rotational performance and negatively affect power generation efficiency. In summary, the optimized blade structural parameters achieve a favorable balance between reducing blade weight, enhancing output current, and improving output voltage.

4. CONCLUSION

This study systematically analyzes the effects of structural parameters of micro wind generator blades on blade weight, generator output current, and output voltage using RSM. Accurate predictive models for these targets were developed, and the NSGA-III algorithm was applied to perform multi-objective optimization. The main findings are as follows:

(1) Single-factor experiments confirm that changes in the root draft angle of micro wind generator blades have negligible effects on generator output current and voltage.

(2) Using the BBD method of RSM, 17 experimental runs were conducted to develop quadratic predictive models for blade weight, generator output current, and output voltage, based on *BD*, *BA*, and *BN*. ANOVA shows that these models are stable and have strong predictive capability.

(3) ANOVA results indicate all three models are statistically significant. The influence of the three structural parameters on generator output current and voltage follows the order: *BN* > *BA* > *BD*. For blade weight, the order is: *BN* > *BD* > *BA*.

(4) Based on the RSM models, the NSGA-III algorithm was used for optimization. The optimal parameters are: *BD* 103 mm, *BA* 35.92°, and 6 blades. The corresponding predicted generator output current is 12.2677 mA, output voltage is 721.9479 mV, and blade weight is 14.9191 g.

(5) Experimental validation using the optimized parameters, yields a generator output current of 11.95 mA, output voltage of 720 mV, and blade weight of 14.6152 g. Compared with results from the RSM experimental group, these findings confirm that the optimized structural parameters produce high output current and voltage with a relatively low blade weight, supporting the effectiveness of the optimization approach.

(6) The prediction errors for output current, output voltage, and blade weight are 2.59%, 2.04%, and 0.27%, respectively, demonstrating the high accuracy of the multi-objective optimization approach integrating RSM and NSGA-III. This method is applicable to similar analysis and prediction problems.

(7) Future work will include blade shape optimization, upscaling to larger generators, and integrated aerodynamic-electromagnetic analysis. Additional studies will consider comparisons with vertical-axis designs, the use of advanced materials, environmental and durability testing, FSI simulations, and cost-effectiveness evaluation to further improve performance and practical application.

ACKNOWLEDGEMENTS

This work is supported by the Anhui Provincial Natural Science Foundation in Universities of China (Grant Nos. 2023AH052937, 2024AH051163); the Anhui Province Provincial Teaching Research Project in Universities of China (Grant No. 2022jyxm969); the Bengbu University application-oriented project of China (Grant Nos. 2024YYX01QD, 2024YYX04QD, 2024YYX03QD).

CONFLICT OF INTEREST

The authors have no conflicts to disclose.

AUTHORS CONTRIBUTION

C. Wang: Methodology, Writing Conceptualization, original draft, Literature survey. **D. Y. Luo**: Methodology, Software, Validation, Data Curation. **H. L. Fan**: Methodology, Software. **H. Yang**: Writing review & editing. **T. L. Wei**: Conceptualization, Writing review & editing.

REFERENCES

Akour, S. N., Al-Heymari, M., Ahmed, T., & Khalil, K. A. (2018). Experimental and theoretical investigation of micro wind turbine for low wind

speed regions. *Renewable Energy*, *116*(Part A), 215–223. https://doi.org/10.1016/j.renene.2017.09.076

Araújo, F. R. P. d., Pereira, M. G., Freitas, M. A. V., da Silva, N. F., & Dantas, E. J. d. A. (2021). Bigger is not always better: Review of small wind in Brazil. *Energies*, *14*(4), 976. https://doi.org/10.3390/en14040976

Bourne, M., Arjomandi, M., & Kurji, R. (2013). The economic assessment of micro wind turbines for South Australia. *Energy Systems*, *4*, 355–377. https://doi.org/10.1007/s12667-013-0081-5

De Oliveira, U. W., Francescatto, M. B., & Roos, C. (2021). Viabilidade econômica de microgeradores eólicos para residências unifamiliares. *Brazilian Journal of Business*, *3*(4), 2838–2850. https://doi.org/10.34140/bjbv3n4-006

Deb, K., & Jain, H. (2014). An evolutionary many-objective optimization algorithm using reference-point-based nondominated sorting approach, Part I: Solving problems with box constraints. *IEEE Transactions on Evolutionary Computation*, *18*(4), 577-601. https://doi.org/10.1109/TEVC.2013.2281535

Deng, S., Cheng, X., Wu, H., & Hu, Y. (2024). Multi-objective optimization of bias current coefficient based on NSGA-III for active magnetic bearing with redundant electromagnetic actuators. *Engineering Computations*, *41*(6), 1549-1571. https://doi.org/10.1108/EC-03-2023-0127

Gu, Q., Xu, Q., & Li, X. (2022). An improved NSGA-III algorithm based on distance dominance relation for many-objective optimization. *Expert Systems with Applications*, *207*, 117738. https://doi.org/10.1016/j.eswa.2022.117738

Huda, S. M. A., Arafat, M. Y., & Moh, S. (2022). Wireless Power Transfer in Wirelessly Powered Sensor Networks: A Review of Recent Progress. *Sensors*, *22*(8), 2952. https://doi.org/10.3390/s22082952

Kumar, N., & Prakash, O. (2023). Analysis of wind energy resources from high rise building for micro wind turbine: A review. *Wind Engineering*, *47*(1), 190–219. https://doi.org/10.1177/0309524X221118684

Leung, D. Y. C., Deng, Y., & Leung, M. K. H. (2011). Parametric study of a fan-bladed micro-wind turbine. *Proceedings of the Institution of Mechanical Engineers, Part A: Journal of Power and Energy*, *225*(8), 1120-1131. https://doi.org/10.1177/0957650911413974

Li, Q., Wang, Y., Li, X., Li, X., Zhang, G., Du, Y., & Xu, W. (2024). Investigation and optimization of textured water-lubricated journal bearings using multi-objective optimization. *Journal of Applied Fluid Mechanics*, *17(9)*, 1912-1928. https://doi.org/10.47176/jafm.17.9.2581

Liu, Q., Liu, X., Wu, J., & Li, Y. (2019). An improved NSGA-III algorithm using genetic k-means clustering algorithm. *IEEE Access*, *7*, 185239-185249. https://doi.org/10.1109/ACCESS.2019.2960531

Maleki, E., Unal, O., & Kashyzadeh, K. R. (2021). Influences of shot peening parameters on mechanical properties and fatigue behavior of 316 L steel: experimental, Taguchi method and response surface methodology. *Metals and Materials International*, *27*, 4418–4440. https://doi.org/10.1007/s12540-021-01013-7

Marin, A., Kishore, R., Schaab, D., Vuckovic, D. & Priya, S. (2016). Micro Wind Turbine for Powering Wireless Sensor Nodes. *Energy Harvesting and Systems*, *3*(2), 139-152. https://doi.org/10.1515/ehs-2013-0004

Mi, S., Liu, J., Cai, L., & Xu, C. (2024). Multi-objective optimization of two-phase ice slurry flow and heat transfer characteristics in helically coiled tubes with RSM and NSGA-II. *International Journal of Thermal Sciences*, *199*, 108942. https://doi.org/10.1016/j.ijthermalsci.2024.108942

Minhas, N., Thakur, A., Mehlwal, S., Verma, R., Sharma, V. S., & Sharma, V. (2021). Multi-variable optimization of the shot blasting of additively manufactured AlSi10Mg plates for surface roughness using response surface methodology. *Arabian Journal for Science and Engineering*, *46*, 11671–11685. https://doi.org/10.1007/s13369-021-05654-z

Miranda, C., Basso, A. D., Francucci, G. M., & Ludueña, L. N. (2022). Design of blades for household small wind turbines. *International Journal of Energy and Environmental Engineering*, *13*, 621–642. https://doi.org/10.1007/s40095-021-00464-3

Ramírez-Elías, V. A., Damian-Escoto, N., Choo, K., Gómez-Martínez, M. A., Balvantín-García, A., & Diosdado-De la Peña, J. A. (2022). Structural analysis of carbon fiber 3D-printed ribs for small wind turbine blades. *Polymers*, *14*(22), 4925. https://doi.org/10.3390/polym14224925

Rocha, P. A., de Araujo, J. W. C., Lima, R. J. P., da Silva, M. E. V., Albiero, D., de Andrade, C. F., & Carneiro, F. O. M. (2018). The effects of blade pitch angle on the performance of small-scale wind turbine in urban environments. *Energy*, *148*, 169–178. https://doi.org/10.1016/j.energy.2018.01.096

Sant, T., Farrugia, R. N., Muscat, M., Caruana, C., Axisa, R., Borg, A., Cassar, C. M., Cassar, J., Cordina, C., Farrugia, A., & Schembri, S. (2020). Development and performance testing of a small, multi-bladed wind turbine. *Wind Engineering*, *44*(1), 3–20. https://doi.org/10.1177/0309524X19849845

Sharma, S., Gupta, V., & Mudgal, D. (2023). Parametric experimental investigation of additive manufacturing-based distal ulna bone plate: a response surface methodology-based design approach. *Rapid Prototyping Journal*, *29*(5), 1080–1096. https://doi.org/10.1108/RPJ-06-2022-0205

Shen, X., Yang, H., Chen, J., Zhu, X., & Du, Z. (2016).

Aerodynamic shape optimization of non-straight small wind turbine blades. *Energy Conversion and Management*, *119*, 266–278. https://doi.org/10.1016/j.enconman.2016.04.008

Sunderland, K. M., Narayana, M., Putrus, G., Conlon, M. F., & McDonald, S. (2016). The cost of energy associated with micro wind generation: international case studies of rural and urban installations. *Energy*, *109*, 818–829. https://doi.org/10.1016/j.energy.2016.05.045

Suresh, A., Raja Kumar, S., Aljafaric, B., & Thanikanti, S. B. (2024). Investigations of the performance of 3D printed micro wind turbine composed of PLA material. *Heliyon*, *10*(3), e25356. https://doi.org/10.1016/j.heliyon.2024.e25356

Tiam Kapen, P., Medjo Nouadje, B. A., Tchuen, G., & Tchinda, R. (2020). Numerical simulation of micro wind turbine performance and efficiency for low wind speed Cameroonian's cities. *International Journal of Ambient Energy*, *43*(1), 2727–2741. https://doi.org/10.1080/01430750.2020.1768894

Umar, M., Jame, N., & Nayan, N. M. (2020). Effect of different types of blades on miniature wind turbine energy harvesting output. *Journal of Physics: Conference Series*, *1432*, 012053. https://doi.org/10.1088/1742-6596/1432/1/012053

Vedovelli, M., Eltayesh, A., Natili, F., & Castellani, F. (2022). Experimental and numerical investigation of the effect of blades number on the dynamic response of a small horizontal-axis wind turbine. *Energies*, *15*(23), 9134. https://doi.org/10.3390/en15239134

Wang, Y., Wang, G., Yao, G., Shen, Q., Yu, X., & He, S. (2023). Combining GA-SVM and NSGA-III multi-objective optimization to reduce the emission and fuel consumption of high-pressure common-rail diesel engine. *Energy*, *278*(Part A), 127965. https://doi.org/10.1016/j.energy.2023.127965

Yu, J., Jin, Z., Yu, Y., Zhao, M., Ma, W., & Wu, J. (2024). Multi-objective optimization of variable-stiffness composite for CFRP-winding buckle arrestor by using NSGA-III. *Marine Structures*, *96*, 103633. https://doi.org/10.1016/j.marstruc.2024.103633

Yu, Y., Pan, Y., Chen, Q., Zeng, D., Hu, Y., Goh, H.-H., Niu, S., & Zhao, Z. (2022). Cogging torque minimization of surface-mounted permanent magnet synchronous motor based on RSM and NSGA-II. *Actuators*, *11*(12), 379. https://doi.org/10.3390/act11120379

Zawadzki, K., Kuzalski, C., Śmiechowicz, W., Tarkowski, M., Kądrowski, D., Stępień, M., Kulak, M., & Lipian, M. (2020). Assessment of blade strength for small wind turbine applications. *E3S Web of Conferences*, *160*, 01007. https://doi.org/10.1051/e3sconf/202016001007

Zhang, Z., Yan, J., Lu, X., Zhang, T., & Wang, H. (2023). Optimization of porosity and surface roughness of CMT-P wire arc additive manufacturing of AA2024 using response surface methodology and NSGA-II. *Journal of Materials Research and Technology*, *24*, 6923–6941. https://doi.org/10.1016/j.jmrt.2023.04.259

Zhao, Y., Cui, L., Sivalingam, V., & Sun, J. (2023). Understanding machining process parameters and optimization of high-speed turning of NiTi SMA using response surface method (RSM) and genetic algorithm (GA). *Materials*, *16*(17), 5786. https://doi.org/10.3390/ma16175786

Zuo, W., Li, D., Li, Q., Cheng, Q., Zhou, K., & E, J. (2023). Multi-objective optimization of multi-channel cold plate under intermittent pulsating flow by RSM and NSGA-II for thermal management of electric vehicle lithium-ion battery pack. *Energy*, *283*, 129085. https://doi.org/10.1016/j.energy.2023.129085